Title

Clonal ZEB1-Driven Mesenchymal Transition Promotes Targetable Oncologic Antiangiogenic Therapy Resistance

Journal

Cancer Research, 80(7)

ISSN

0008-5472

Authors

Chandra, Ankush
Jahangiri, Arman
Chen, William
et al.

Publication Date

2020-04-01

DOI

10.1158/0008-5472.can-19-1305

Peer reviewed

HHS Public Access

Author manuscript

Cancer Res. Author manuscript; available in PMC 2020 October 01.

Published in final edited form as:

Cancer Res. 2020 April 01; 80(7): 1498–1511. doi:10.1158/0008-5472.CAN-19-1305.

Clonal ZEB1-driven mesenchymal transition promotes targetable oncologic anti-angiogenic therapy resistance

Ankush Chandra[1,‡], **Arman Jahangiri**[1,‡], **William Chen**[1,‡], **Alan T. Nguyen**[1], **Garima Yagnik**[1], **Matheus P. Pereira**[1], **Saket Jain**[1], **Joseph H. Garcia**[1], **Sumedh S. Shah**[1], **Harsh Wadhwa**[1], **Rushikesh S. Joshi**[1], **Jacob Weiss**[1], **Kayla J. Wolf**[2], **Jung-Ming G. Lin**[2], **Sören Müller**[1], **Jonathan W. Rick**[1], **Aaron A. Diaz**[1], **Luke A. Gilbert**[3], **Sanjay Kumar**[2], **Manish K. Aghi**[1]

[1]Dept. of Neurosurgery, University of California San Francisco (UCSF)

[2]Dept. of Bioengineering, University of California Berkeley

[3]Dept. of Urology, UCSF

Abstract

Glioblastoma responses to bevacizumab are invariably transient with acquired resistance. We profiled paired patient specimens and bevacizumab-resistant xenograft models pre- and post-resistance towards the primary goal of identifying regulators whose targeting could prolong the therapeutic window, and the secondary goal of identifying biomarkers of therapeutic window closure. Bevacizumab-resistant patient specimens and xenografts exhibited decreased vessel density and increased hypoxia versus pre-resistance, suggesting that resistance occurs despite effective therapeutic devascularization. Microarray analysis revealed upregulated mesenchymal genes in resistant tumors correlating with bevacizumab treatment duration and causing three changes enabling resistant tumor growth in hypoxia. First, perivascular invasiveness along remaining blood vessels, which co-opts vessels in a VEGF-independent and neo-angiogenesis-independent manner, was upregulated in novel biomimetic 3D bioengineered platforms modeling the bevacizumab-resistant microenvironment. Second, tumor-initiating stem cells housed in the perivascular niche close to remaining blood vessels were enriched. Third, metabolic reprogramming assessed through real-time bioenergetic measurement and metabolomics upregulated glycolysis and suppressed oxidative phosphorylation. Single-cell sequencing of bevacizumab-resistant patient glioblastomas confirmed upregulated mesenchymal genes, particularly glycoprotein YKL-40 and transcription factor ZEB1, in later clones, implicating these changes as treatment-induced. Serum YKL-40 was elevated in bevacizumab-resistant vs. bevacizumab-naïve patients. CRISPR and pharmacologic targeting of ZEB1 with honokiol reversed the mesenchymal gene expression and associated stem cell, invasion, and metabolic changes defining resistance. Honokiol caused greater cell death in bevacizumab-resistant than bevacizumab-responsive tumor cells, with surviving cells losing mesenchymal morphology. Employing YKL-40 as a resistance biomarker and ZEB1 as a target to prevent resistance could fulfill the promise of anti-angiogenic therapy.

Corresponding author: Manish K. Aghi, MD, PhD; Professor of Neurosurgery; UCSF; Diller Cancer Research Building; 1450 Third Street HD-465; San Francisco, CA 94158; 415-353-1172; FAX=415-353-3907; manish.aghi@ucsf.edu.

‡Contributed equally

The authors declare no potential conflicts of interest.

Graphical Abstract

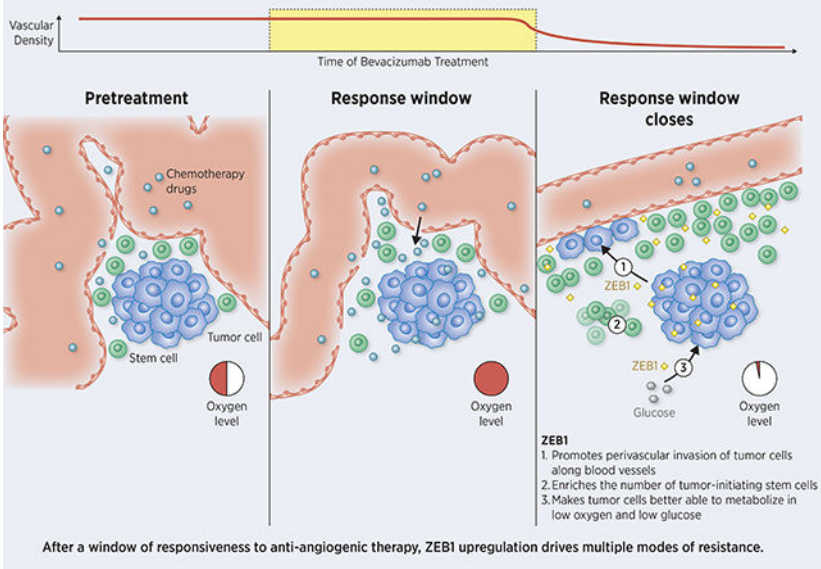

Keywords

bevacizumab; glioblastoma; mesenchymal; invasion; xenograft; ZEB1

INTRODUCTION

Based on encouraging clinical trial results (1), bevacizumab, a humanized antibody targeting vascular endothelial growth factor (VEGF), is approved as monotherapy for recurrent glioblastoma (GBM), an aggressive brain malignancy with 90% mortality three years after diagnosis (2). Unfortunately, bevacizumab responses are typically transient, with 50% of GBMs that initially respond progressing soon thereafter (1), with acquired bevacizumab resistance associated with poor outcomes (3). Indeed, phase III trials of bevacizumab in newly diagnosed (4,5) and recurrent (6) GBM revealed increased progression free survival (PFS) but unchanged overall survival (OS).

While some studies have suggested that anti-angiogenic therapy resistance involves upregulated compensatory VEGF-independent angiogenesis (7,8), others have suggested that resistance involves changes enabling tumor cells to thrive in the hypoxic microenvironment of a successfully devascularized tumor (9,10). Resolving these discordant findings requires comprehensive study of the microenvironment of these resistant tumors. To address this knowledge gap in a manner accounting for the impact of treatment duration which can be prolonged in patients compared to *in vivo* studies in mice, we analyzed paired specimens from patients before and after tumor progression on variable duration of bevacizumab treatment and in two GBM xenograft models of bevacizumab resistance created by our group (11). These tissues were analyzed for serial treatment-associated changes in hypoxia and vascularity. We also used bulk and single-cell transcriptomics to screen for biomarkers of therapeutic window closure and regulators particularly upregulated

in late clones associated with therapeutic resistance (12) whose targeting could prolong the bevacizumab therapeutic window in GBM.

MATERIALS AND METHODS

Cell Culture

HUVEC cells (ATCC) verified using short tandem repeat (STR) profiling were passaged under 6 times and cultured in EGM-2 (Lonza). Bevacizumab-sensitive and resistant U87-Bev^S/U87-Bev^R and patient-derived (Supplementary Table S1) xenografts were generated and cells for culture extracted as described (13,14), confirmed Mycoplasma-free, and cultured in DMEM/F-12 plus 10% FBS and 1% P/S at 37°C, with some cells treated with 20 μM honokiol (Sigma). For survival studies, trypan blue exclusion viability assay was performed (15). U87-Bev^S, U87-Bev^R and primary GBM neurospheres were cultured in Neurocult/Neurosphere media (StemCell Technologies) with 10 ng/ml bFGF (Thermo Fisher), 20 ng/ml EGF (Thermo Fisher) and B27 and N2 supplement (Thermo Fisher) at 37°C. Accutase (StemCell Technologies) was used to dissociate neurospheres into single cell suspensions.

Animals

Animal experiments approved by UCSF IACUC (approval #AN105170–02) are in Supplementary Methods.

Morphology Analysis

Morphology and form factor analyses were performed as described previously (11) and in Supplementary Methods.

Generation of Neurospheres and Functional Assays

See Supplementary Methods

Human Serum ELISA

See Supplementary Methods

CRISPR knockout

ZEB1 was knocked out in U87-Bev^S, U87-Bev^R generations 1,4 and 9 by co-transfecting ZEB1 CRISPR/Cas9 KO and ZEB1 HDR Plasmids (sc-400201 and sc-400201-HDR; Santa Cruz Biotechnology, CA) using FuGENE® 6 Transfection Reagent (Promega). Transfections were done per manufacturer instructions, and verified using qPCR and microscopy for Red Fluorescent Protein (RFP).

Microarrays

Previously flash frozen generational xenograft tumor chunks were retrieved and dissociated using a QiaShredder (Qiagen) and passage through a 21-gauge sterile syringe. Dissociated tissue was processed to obtain RNA using the RNeasy kit (Qiagen), following manufacturer’s protocol. RNA quality was tested using an RNA 6000 chip with the

Bioanalyzer hardware (Agilent). RIN scores>8 were required for RNA quality. RNA was converted to labeled cRNA using the TargetAmp-Nano Labelling Kit for Illumina Expression BeadChip (EpiCentre), following manufacturer's protocol. Labelled cRNA was kept at −20°C and given to the UCSF Genome Core Facility (GCF) for chip hybridization.

Single-cell RNA sequencing

Tissue was dissociated by incubation in papain with 10% DNAse for 30 min. A single-cell suspension was obtained by manual trituration using a glass pipette. Cells were filtered via an ovomucoid gradient to remove debris, pelleted, and resuspended in Neural Basal Media with serum at 1700 cells/μL, with 10.2 μL cells loaded into each well of a 10X Chromium Single-Cell capture chip and two lanes captured. Single-cell capture, reverse transcription, cell lysis, and library preparation were performed per manufacturer's protocol. Sequencing was performed on a HiSeq 2500 (Illumina, 100-bp paired-end protocol). Raw data was processed with CellRangeR 1.3. The resulting count table derived from CellRangeR was processed in R 3.4.1. Data normalization (log (CPM/100+1) and subsequent t-SNE clustering was performed with the Seurat R package (16). Copy number inference was carried out with the CONICSmat R package (https://github.com/diazlab/CONICS/) (17). Only tumor cells harboring at least one clonal mutation (chr10 loss or chr7 gain, determined by thresholding the posterior probability of the mixture model, pp<0.05) were accounted for in t-SNE clustering. For each clone, we detected genes specific to early (2–3 mutations) or late (>3 mutations) clones (P<0.05, t-test with Benjamini-Hochberg correction and log FC>0.3). We used Opossum (18) to calculate transcription factor binding motif enrichment in the gene sets specific to each clone set (Fisher test). The most significant enrichments were visualized in a bar graph.

Bioinformatics

GCF analysis of xenograft arrays (.idat files) were processed through the UCSF Bioinformatics Core and deposited in GEO (Accession number=GSE81465). We accessed our archived (19) microarray analysis of BRGs and their paired pre-treatment GBMs from ArrayExpress (accession no.=E-MEXP-3296). To identify significantly dysregulated genes across generations, a two-component normal mixture-model was fitted by expectation-maximization to the Z-transformed Log(variance) distribution of gene expression values over generations 4 and 9. A posterior probability cutoff (≥0.95) (20) yielded 717 significantly dysregulated genes. Next, a non-parametric bootstrap procedure (21) was performed using MATLAB in order to determine if our data over-represented the Philips mesenchymal, proneural, and proliferative gene sets among these dysregulated genes. Microarray probes were mapped to HGNC gene names, and uniform random sampling of 717 of the 48,324 gene probes followed by matching to the mesenchymal, proneural, or proliferative gene sets was repeated 50,000 times, resulting in a putative null distribution of the number of matches to each gene set. A Poisson probability density function was fit by maximum likelihood estimation to this distribution and a 1-tailed p-value calculated for the observed number of matches to the gene set in question. Genes were further clustered by k-means clustering based on gene expression trajectory across generations, and these expression trajectory clusters were manually curated into upregulated genes (sustained increases in expression through generation 4–9), downregulated genes (sustained decreases

in expression through generation 4–9), and other genes. Expression of particular genes identified from microarrays was validated using qPCR.

Quantitative PCR

After obtaining RNA in triplicate from xenografts as described in the microarray analysis, cDNA was created using qScript XLT cDNA Supermix (Quanta Bio), following manufacturer's protocol. cDNA was diluted to a constant concentration for all samples to ensure similar nucleic acid loading. Quantitative PCR was carried out using Power Syber Green Master Mix (Applied Biosystems), primer sequences in Supplementary Tables S2–S4, and an Applied Biosystems StepOne Real-Time PCR cycler following Applied Biosystems Syber guidelines: 95°C for 10 min, followed by 40 cycles of 95°C/15 sec and 60°C/1 min. Ct values were calculated using StepOne software (Applied Biosystems).

Microchannel Device Fabrication

See Supplementary Methods.

Cell Motility Measurements in Microchannel Device

Live-cell imaging was performed using a Nikon Ti-E2000-E2 microscope equipped with a motorized, programmable stage (Applied Scientific Instrumentation), an incubator with constant temperature, humidity, and CO2 (In vivo Scientific), a digital camera (Photometrics CoolSNAP HG II), and NIS Elements (Nikon) software. Images were taken at 5 ms exposure, 2×2 pixel binning using a 10x-objective (Nikon CFI Plan Fluor DLL). Cell motility was measured using phase contrast time-lapse images acquired every 15 minutes over three hours. ImageJ software (NIH) was used to track cell centroids from one frame to another to yield migration speeds, which were averaged over the experiment to yield the migration speed of a cell. Cells sticking to each other were excluded.

HA Matrix Synthesis and Invasion Device Fabrication

See Supplementary Methods.

Invasion and Protrusion Analysis

For area analysis in HA devices, cells in devices were imaged every 3 days using Eclipse TE2000 Nikon Microscope with a Plan Fluor Ph1 10x objective. Images were acquired and stitched using NIS-Elements Software. For each device, total cell area was outlined in ImageJ and normalized to total day 1 cell area. To analyze morphology, invading edge protrusions were counted and normalized to cell mass length.

Dye transfer studies

See Supplementary Methods.

Colorimetric metabolic assays

Pyruvate concentrations, glucose uptake, glycolysis rates, and ATP levels were measured as described (9) and in Supplementary Methods.

Seahorse extracellular flux analyzer

See Supplementary Methods.

Metabolomics

See Supplementary Methods

Statistics

Student's t-test and Mann-Whitney tests were used to compare means of continuous parametric and non-parametric variables, respectively. Paired t-tests (parametric) and Wilcoxon signed-rank tests (non-parametric) were used to compare pre- and post-treatment variables from the same patients. Interobserver variability for manual immunofluorescence counting was assessed using SPSS VARCOMP analysis. Multiple comparisons used ANOVA followed by Tukey Kramer multiple comparisons test. *P* values are two-tailed and $P<0.05$ was significant.

RESULTS

Bevacizumab resistance occurs despite successful devascularization correlating with treatment duration in patients and xenograft models

We investigated the impact of bevacizumab treatment duration on patient bevacizumab-resistant glioblastomas (BRGs). Immunohistochemistry for hypoxia marker CA9 and endothelial antigen CD31 revealed that increasing bevacizumab treatment duration before progression increased BRG hypoxia (Fig. 1a; $R^2=0.63$; P=0.004) and decreased vessel density (Fig. 1b; $R^2=0.66$; P=0.002), without affecting Ki-67 labeling (Fig. 1c; $R^2=0.01$; P=0.7). We found similar hypoxic devascularization in two models of bevacizumab resistance established by our group. The first model transfers the effects of prolonged anti-angiogenic therapy from the patient to the mouse via patient-derived xenografts (PDXs) that maintain the sensitivity or resistance to bevacizumab of the original patient tumor, while the second model uses a multi-generational approach to painstakingly recapitulate in mice the prolonged anti-angiogenic therapy that preceded resistance in patients (13,14).

For our xenograft model based on PDXs, intracranial bevacizumab-responsive PDXs (SF8244; Supplementary Table S1) exhibited decreased vessel density (P=0.02; Fig.1d) and increased hypoxia (P=0.01; Fig. 1e) in response to bevacizumab but bevacizumab-resistant PDXs (SF7796 and SF8106; Supplementary Table S1) were devascularized and hypoxic at baseline and those parameters did not change in response to bevacizumab (P=0.5–0.9; Fig. 1d–e). We also found corroborative xenograft evidence that bevacizumab resistant GBMs became hypoxic and devsascularizaed in our second model of bevacizumab resistance, U87-Bev^R (Fig. S1). During its multi-generational ectopic subcutaneous creation, U87-Bev^R exhibited decreased vessel density (P<0.01; Fig. S2) and increased hypoxia (P<0.001; Fig. S3) without altering proliferation (P=0.07; Fig. S4) relative to responsive U87-Bev^S xenografts. The same finding occurred when we implanted the final generation of U87-Bev^R and U87-Bev^S in the orthotopic intracranial microenvironment, where decreased vessel density (P=0.03; Fig. 1f) and increased hypoxia (P=0.001; Fig. 1g) were noted with bevacizumab treatment of intracranial bevacizumab-sensitive U87-Bev^S xenografts, while

intracranial bevacizumab-resistant U87-Bev^R xenografts were devascularized and hypoxic at baseline and those parameters did not change in response to bevacizumab (P=0.1–0.6; Fig. 1f–g). Thus, patient BRGs and our xenograft models exhibited increased hypoxia with decreased vessel density with increasing bevacizumab treatment duration but maintain their proliferative indices despite this therapy-induced harsh microenvironment, suggesting that BRGs grow despite successful bevacizumab-induced devascularization.

Resistance to bevacizumab monotherapy is associated with mesenchymal progression in a manner correlating with treatment duration in patients and xenograft models

We used our previously published microarray analysis of 15 BRGs relative to paired pre-treatment GBMs from the same patients (14,19) to analyze expression of the 35 signature genes used to define GBM subtypes (proneural, mesenchymal, and proliferative) (22). This analysis revealed a tendency for tumors to become more mesenchymal with increasing bevacizumab treatment duration before progression when bevacizumab was used as monotherapy (n=5; P=0.02; Fig. 2a) but not when it was used in combination with traditional chemotherapy (n=10; P=0.1; Fig. S5).

Similarly, our bevacizumab-resistant PDX SF7796 exhibited increased mesenchymal gene expression by qPCR relative to our bevacizumab-responsive PDX GBM43 (P<0.05; Fig. 2b). To serially investigate transcriptional changes associated with bevacizumab resistance evolution, we performed microarray expression analysis of U87-Bev^R generations 1, 4, and 9, a model established with the serial use of bevacizumab monotherapy. Bootstrapping analysis of microarray data revealed that 19 of the 170 genes from the extended lists of mesenchymal subtype markers (11%) (22) were significantly dysregulated across U87-Bev^R generations (P<0.001) and 9 of the 338 genes from the extended list of proneural subtype markers (2%) (22) were dysregulated (P=0.03). Furthermore, 37% of dysregulated mesenchymal genes were upregulated, while 44% of dysregulated proneural genes were downregulated (Fig. 2c–d). These findings were illustrated by a heatmap (Fig. 2e) and a three-dimensional plot created by averaging and normalizing expression of the 14 mesenchymal, 15 proneural, and 5 proliferative genes (22), to obtain mesenchymal, proneural, and proliferative gene expression scores on a +1 to −1 scale (Fig. 2f). The heatmap (Fig. 2e) illustrated early mesenchymal gene upregulation versus early proneural gene downregulation followed by a more modest later rise in proneural gene upregulation, and the three-dimensional plot revealed mesenchymal gene upregulation approaching +1 by generation 4 and persisting thereafter, versus more heterogeneous later changes in proneural gene expression (Fig. 2f). These findings mirrored gene expression changes occurring with increasing bevacizumab treatment duration in patient BRGs. To validate these findings, we performed qPCR for the 14 mesenchymal genes (22) and confirmed increased expression of all but one gene by generation 9 (Fig. 2g).

Resistant tumors exhibit altered morphology and increased perivascular invasiveness

Because our microarray analysis revealed upregulated genes promoting cytoskeletal and extracellular matrix (ECM) re-organization and tumor cell migration (Fig. S6), we investigated bevacizumab-resistant GBM cell invasiveness. We found more stellate morphology (P<0.01; Fig. S7; Fig. 3a) and invasiveness in Matrigel assays (P<0.01; Fig. 3b)

in GBM cells from our bevacizumab-resistant PDX models compared to GBM cells from our bevacizumab-responsive PDX models. Similarly, we found more stellate morphology ($P<0.01$; Fig. S8; Figs. 3c) and invasiveness in Matrigel assays ($P=0.0003–0.04$; Fig. S9; Fig. 3d) in U87-Bev^R versus U87-Bev^S cells, consistent with prior reports (3,13,14,19). We then investigated BRG cell invasion in two different three-dimensional bioengineered models replicating different GBM invasion modes. The first model was hydrogel platforms (23) that model the gray and white matter along which peritumoral invasion occurs and contain the hyaluronic acid (HA) upregulated in bevacizumab-resistant tumor ECM (24). In this hydrogel model, U87-Bev^R cells proved more invasive than U87-Bev^S cells ($P<0.001$; Fig. 3e). The second model was microchannel platforms in which tumor cells start in a tumor-like cell reservoir, which they migrate out of into a 3D matrix of HA conjugated to RGD peptide in a manner that models peritumoral invasion, after which tumor cells migrate through the HA-RGD towards a parallel open channel “vessel” embedded in the 3D HA-RGD matrix in a manner that models perivascular invasion (25). U87-Bev^R cells were also more invasive than U87-Bev^S cells in these microchannel platforms ($P<0.05$; Fig. 3f; Figs. S10–11).

Resistant tumors exhibit increased tumor-initiating stem cells

Because residing in the perivascular niche could enable tumor-initiating stem cells to survive therapy-induced hypoxia (26), we investigated whether patient BRGs exhibited enriched tumor-initiating stem cells. Plating cells from patient BRGs (n=4) versus bevacizumab-naïve recurrent GBMs (n=3) in neurosphere medium that isolates tumor-initiating stem cells revealed increased cell counts from dissociated neurospheres in BRGs versus bevacizumab-naïve GBMs ($P<0.001$; Fig. 4a). Consistent with this finding, our bevacizumab-resistant PDX SF7796 exhibited greater expression of a seven gene stem cell panel (Supplementary Table S2) by qPCR than our bevacizumab-responsive PDX GBM43 ($P<0.05$; Fig. 4b). Similarly, U87-Bev^R tumors exhibited increased expression of this seven gene stem cell panel by qPCR, peaking at generation 4 versus U87-Bev^S tumors ($P<0.01$ for generation 1; $P<0.001$ for generation 4; and $P<0.01$ for generation 9; Fig. 4c). Culturing U87-Bev^R cells in neurosphere medium revealed that, although U87-Bev^R cells formed fewer neurospheres than U87-Bev^S cells, U87-Bev^R neurospheres were larger ($p=0.002$) and more cellular ($p=0.0002$) than U87-Bev^S cells (Fig. 4d–h), reflecting less differentiated, more proliferative stem cells more resistant to hypoxia (27).

Single-cell analysis of gene expression changes associated with bevacizumab resistance to understand resistance ontogeny

To determine whether these changes were arising homogeneously in individual cells or in single cells giving rise to multiple clones, we performed single-cell RNA sequencing of 857 cells from a BRG (Fig. 5a). When focusing on the tumor cells, and moving into the gene space of the 500 most differentially expressed genes identified by our BRG microarray analysis (14), we identified clusters of single cells (Fig. 5a), revealing that BRG cells differ in the expression of these genes. When analyzing these cells for mesenchymal gene expression (Fig. 5b) or copy number variation (Fig. 5c), five clones were identified, a high number indicative of significant evolutionary pressure from bevacizumab. Comparing gene expression of later clones with more mutations to early clones with fewer mutations revealed

similar tumor cell proliferative potential based on KI67 expression (P=0.8 early vs. late clones; Fig. 5d), with a trend towards a proneural to mesenchymal gene expression shift from early to late clones approximating statistical significance (proneural *DLL3* downregulated, P=0.06; mesenchymal *YKL-40* upregulated, P=0.09; Fig. 5d). To identify upstream regulators of these changes, we performed an enrichment test for transcription factor binding sites in the single-cell sequencing data, revealing that ZEB1 binding sites were enriched in genes from early and late clones, with the enrichment p-value more significant in late clones ($P=1.0\times10^{-6}$ vs. $5.1X10^{-8}$ for ZEB1 binding site enrichment in early vs. late clones; Fig. 5e), suggesting that ZEB1 could drive BRG gene expression, particularly in late, presumably more resistant clones.

Mesenchymal gene expression analysis identifies YKL-40 as a serum biomarker of resistance

Our single-cell sequencing revealed early clonal evolution of *YKL-40* upregulation in patient bevacizumab-resistant GBM cells. Consistent with this finding, tumor lysates from our intracranial bevacizumab-resistant SF7796 PDXs exhibited greater *YKL-40* gene expression than lysates from our intracranial bevacizumab-responsive GBM43 PDXs (n=3/group; P<0.001; Fig. S12). Similarly, *YKL-40* gene expression arose by qPCR across tumors from multiple U87-Bev^R generations (P<0.001; Fig. S13). Because YKL-40 is a secreted glycoprotein detectable in the circulation, we investigated YKL-40 as a potential biomarker of bevacizumab-induced mesenchymal change. We measured YKL-40 in sera of BRG (n=8) versus bevacizumab-naïve (n=11) GBM patients immediately pre-operatively and found elevated serum YKL-40 in BRG patient serum versus serum from recurrent bevacizumab-naïve GBMs (P<0.05; Fig. 5f).

ZEB1 drives BRG mesenchymal morphology and stem-like changes

We investigated the role of *ZEB1*, an upregulated gene in our single-cell sequencing expressing a transcription factor associated with the stem cells and mesenchymal change we identified with bevacizumab resistance (28–30), in the resistant phenotype. We found a trend of increased *ZEB1* gene expression by qPCR across generations of U87-Bev^R xenografts compared to U87-Bev^S xenografts ($P=1X10^{-5}$-0.02; Fig. 6a). Using CRISPR to disrupt *ZEB1* expression in generations 1, 4, and 9 of U87-Bev^R and U87-Bev^S (Fig. S14; Fig. 6b) caused complete loss of the mesenchymal gene expression (P<0.001; Fig. 6c), altered morphology (P<0.001; Fig. 6d; Fig. S15), and parenchymal (P<0.001; Fig. S16) and perivascular (P<0.001 protrusion density and P<0.05 invasion area; Fig. 6e) invasiveness seen in U87-Bev^R cells. The role of perivascular invasiveness in bevacizumab resistance has been hypothesized to be due to it serving as a form of VEGF-independent angiogenesis that provides tumor cells with nutrients through direct transfer from tumor cell contact with endothelial cells. Along those lines, CRISPR-mediated ZEB1 knockout in U87-Bev^R cells reduced calcein dye transfer from HUVEC endothelial cells to tumor cells (P=0.01; Fig. 6f) and reduced expression of tumor cell connexins (P<0.001; Fig. 6g) that form gap junctions facilitating nutrient transfer between endothelial and tumor cells (31). ZEB1 knockout in U87-Bev^R also reversed the stem cell changes we noted in U87-Bev^R cells, by decreasing their expression of the stem cell gene panel described earlier (P<0.001; Fig. 6h), stem cell

counts (P<0.001; Fig. 6i), stem cell diameters (P<0.001; Fig. 6j), and neurosphere yield (P<0.001; Fig. S17).

ZEB1 drives metabolic changes associated with bevacizumab resistance

Another aspect of the mesenchymal changes we noted that is a crucial component of how bevacizumab-resistant tumor cells thrive in the hypoxic devascularized microenvironment we describe here (Fig. 1) is metabolic reprogramming enhanced the Warburg effect. Using qPCR, we found increased expression of the GLUT3 glucose transporter, which we reported to drive metabolic reprogramming during bevacizumab resistance (9), in U87-Bev^R tumors compared to U87-Bev^S tumors (P<0.001 generation four and P<0.01 generation nine; Fig. S18). Consistent with a lung cancer study (29), targeting ZEB1 with CRISPR in U87-Bev^R shut down GLUT3 expression assessed by qPCR (P<0.001; Fig. 7a) and western blot (Fig. 7b). Similarly, pharmacologically targeting ZEB1 with honokiol, a natural phenolic compound from seed cones that inhibits STAT3-mediated ZEB1 transcription (32), in U87-Bev^R cells reversed their elevated ZEB1 (P<0.05) and GLUT3 (P<0.05) expression (Fig. S19). These findings suggested that ZEB1 was driving the GLUT3 expression that we have shown promotes the metabolic reprogramming of bevacizumab resistance. Consistent with this regulatory role of ZEB1 in metabolic changes associated with bevacizumab resistance, principal component analysis (PCA) of metabolites generated when U87-Bev^R and U87-Bev^S cells expressed CRISPR targeting ZEB1 or control (CTL) sequences were incubated in a low concentration (0.1 g/L) of $^{\mathbf{13}}C_6$-glucose revealed identical metabolite profile between U87-Bev^S expressing CTL vs. ZEB1 CRISPR, while ZEB1 CRISPR reversed many metabolite changes seen in U87-Bev^R, driving them towards the metabolite profile of U87-Bev^S (Fig. S20). ZEB1 CRISPR also decreased glucose uptake (P<0.001; Fig. 7c; Fig. S21), decreased glycolysis (P<0.001; Fig. 7d; Fig. S22), and decreased ATP production (P<0.001; Fig. 7e; Fig. S23) in U87-Bev^R cells. We then used the Seahorse extracellular flux analyzer to dynamically assess oxygen consumption as a measure of oxidative phosphorylation and found that ZEB1 CRISPR increased the oxidative phosphorylation of U87-Bev^R cells (P=0.002–0.008; Fig. 7f) at baseline (pre-injection 1) and during maximal respiration (post-FCCP) phases of the assay. Similarly, metabolomic comparison of U87-Bev^R CTL CRISPR and U87-Bev^R ZEB1 CRISPR cells in 0.1 g/L $^{\mathbf{13}}C_6$-glucose revealed increased tricarboxylic acid (TCA) cycle intermediate metabolites in ZEB1 CRISPR cells, resembling the metabolic profile of U87-Bev^S cells (Fig. 7g). The translational impact of targeting ZEB1 in bevacizumab-resistant GBM was defined when honokiol proved more cytotoxic when treating U87-Bev^R cells than U87-Bev^S cells (P<0.05; Fig. 7h) and reversed the mesenchymal morphology of surviving U87-Bev^R cells (P<0.001; Figs. S24 and 7i).

DISCUSSION

The failure of anti-angiogenic agents like bevacizumab to achieve durable response in GBM (4) and other cancers (33) has led to debate about whether acquired bevacizumab resistance involves lost anti-angiogenic effect due to compensatory upregulation of VEGF-independent angiogenesis pathways (7) or tumor adaptation to a devascularized microenvironment. We found in patient specimens and two novel xenograft models that BRGs exhibited hypoxia and devascularization that worsened with increasing treatment duration, indicating that the

resistance occurs despite continued successful bevacizumab-induced devascularization. In some ways, our findings contrast with work of Jain and colleagues which demonstrated vascular normalization after anti-angiogenic therapy (34). It is possible that our findings of therapy-induced devascularization in resistant tumors arise because prolonged anti-angiogenic therapy beyond the duration of treatment needed to achieve vascular normalization leads to closure of the vascular normalization window. Further study would be needed to confirm this hypothesis, but it would be consistent with reports of greater bevacizumab effectiveness in tumors with greater starting vascularization (35) or milder therapy-induced devascularization (36), suggesting that excessive vascular pruning or rarefaction after bevacizumab therapy may negatively impact patient outcomes.

Our work revealed three adaptive changes in GBM in response to bevacizumab-induced hypoxic devascularization: perivascular invasion, enrichment of tumor-initiating stem cells, and metabolic reprogramming. Using 3D bioengineered systems customized to reflect the ECM remodeling shown to occur in bevacizumab-resistant GBM (24), we demonstrated increased invasiveness, including perivascular invasiveness, in bevacizumab-resistant cells. Invasiveness after bevacizumab resistance has been described as perivascular, which supports tumor cells because the perivascular space is the entry point for nutrients into the brain (37–39). By invading alongside and engulfing preexisting cerebral microvasculature, perivascular invasion co-opts existing vasculature in a VEGF-independent and neo-angiogenesis-independent manner (40), providing a mechanism for continued GBM growth despite the VEGF blockade mediated tumor de-vascularization. Concomitant with this increased invasiveness, we found that the transcriptional changes during bevacizumab resistance enriched tumor-initiating stem cells, progenitor cells resistant to hypoxia both at a cellular level and due to these cells residing in the GBM perivascular niche (26), and described as enriched in other studies of anti-angiogenic therapy resistance (41). A metabolic switch to glycolysis and away from oxidative phosphorylation is another adaptation of GBM to the hypoxia exacerbated by bevacizumab, as glycolysis enables more efficient ATP production (9,42).

We found that mesenchymal change was crucial to these phenotypic changes in xenografts and patient specimens. Our work thus expands upon xenograft studies in which tumor treatment with anti-VEGF antibody promotes increased transcription of mesenchymal factors that portend a worse prognosis in GBM and other cancers (43,44). GBM molecular subtypes have been defined based on similarity to defined expression signatures. To study subtype changes associated with bevacizumab resistance, we chose the Phillips classification (22) rather than the Verhaak classification (45) because the former uses more focused gene sets that change during GBM evolution. Using this classification, we demonstrated mesenchymal change in our xenograft models which mirrored our finding of increased mesenchymal gene expression with longer bevacizumab treatment duration in patient BRGs. Beyond anti-angiogenic therapy, our work adds to studies implicating mesenchymal gene expression in resistance to other anti-cancer therapies such as radiation in GBM (46) and EGFR inhibitors in lung cancer (47). These mesenchymal changes confer context-dependent advantages particular to the therapy that resistance is evolving against. Specifically, radiation resistance arises due to enhanced DNA damage repair in mesenchymal cells, EGFR-targeted therapy resistance arises due to the intrinsic refractoriness of signaling pathways to down-

regulation in mesenchymal cells, and anti-angiogenic therapy resistance arises due to the perivascular invasion, stem cell enrichment, and metabolic changes we found associated with mesenchymal change in GBM. Thus, mesenchymal gene expression not only promotes resistance to anti-angiogenic therapy but promotes a phenotype resistant to multiple therapeutic modalities.

To identify a clinically translatable biomarker of when the response window to bevacizumab may close and a translatable target that could prevent resistance, we analyzed bevacizumab resistance genes at a single-cell level. We found that mesenchymal gene expression was more prevalent in late BRG clones, implicating these changes as therapy-related because late clones identified in single-cell sequencing have been associated with therapeutic resistance (12). Further analysis of these late clones revealed that the resistant state had an associated biomarker in elevated serum glycoprotein YKL-40 in BRG patients and revealed transcription factor ZEB1 to be a promising regulator of mesenchymal change during bevacizumab resistance evolution. Targeting ZEB1 with CRISPR and honokiol disrupted bevacizumab resistance features and caused preferential toxicity in resistant cells. While our study is the first to implicate ZEB1 as a bevacizumab resistance driver, serum YKL-40 elevation during bevacizumab treatment of ovarian cancer patients predicts shorter PFS (48) and low baseline YKL-40 was associated with improved outcomes in ovarian cancer (48) and GBM (49) patients receiving bevacizumab. Because honokiol could exert ZEB1-independent effects via inhibition of STAT3 (32), our honokiol findings are not as directly implicative of ZEB1's role in bevacizumab resistance as our CRISPR findings. Regardless, because bevacizumab resistance has been challenging to pharmacologically target (50), these findings and the ability to screen inhibitors of bevacizumab resistance in our models or other confirmatory isogeneic bevacizumab resistance models, that could be similarly established, to improve upon our work, which was done in a single isogeneic resistance model before validating in PDXs and patient specimens, could provide meaningful benefit to GBM patients.

Supplementary Material

Refer to Web version on PubMed Central for supplementary material.

ACKNOWLEDGEMENTS

M.K.A. was supported by the American Brain Tumor Association, McDonnell Foundation, American Cancer Society, University of California Cancer Research Coordinating Committee, and NIH (1R01CA227136 and 2R01NS079697). A.C., A.J., J.R., and S.S. received Howard Hughes Medical Institute fellowships. A.C. received an Alpha Omega Alpha Carolyn L. Kuckein Student Research Fellowship. A.J. received an NIH Predoctoral Fellowship 1F31CA203372. W.C., J.H.G. and J.R. received UCSF School of Medicine Pathways Explore Grants. K.J.W. received an NSF Predoctoral Fellowship. S.K. received NIH funding (1R21CA174573, 1R01GM122375, 1R21EB025017). UCLA Metabolomics Center performed metabolomics studies. The Seahorse analyzer was gifted from the S.D. Bechtel Junior Foundation to the Gladstone Institutes.

REFERENCES

1. Kreisl TN, Kim L, Moore K, Duic P, Royce C, Stroud I, et al. Phase II trial of single-agent bevacizumab followed by bevacizumab plus irinotecan at tumor progression in recurrent glioblastoma. J Clin Oncol 2009;27:740–5 [PubMed: 19114704]

2. Luo JW, Wang X, Yang Y, Mao Q. Role of micro-RNA (miRNA) in pathogenesis of glioblastoma. European review for medical and pharmacological sciences 2015;19:1630–9 [PubMed: 26004603]
3. Clark AJ, Lamborn KR, Butowski NA, Chang SM, Prados MD, Clarke JL, et al. Neurosurgical management and prognosis of patients with glioblastoma that progresses during bevacizumab treatment. Neurosurgery 2011;70:361–70
4. Chinot OL, Wick W, Mason W, Henriksson R, Saran F, Nishikawa R, et al. Bevacizumab plus radiotherapy-temozolomide for newly diagnosed glioblastoma. N Engl J Med 2014;370:709–22 [PubMed: 24552318]
5. Gilbert MR, Dignam JJ, Armstrong TS, Wefel JS, Blumenthal DT, Vogelbaum MA, et al. A randomized trial of bevacizumab for newly diagnosed glioblastoma. N Engl J Med 2014;370:699–708 [PubMed: 24552317]
6. Taal W, Oosterkamp HM, Walenkamp AM, Dubbink HJ, Beerepoot LV, Hanse MC, et al. Single-agent bevacizumab or lomustine versus a combination of bevacizumab plus lomustine in patients with recurrent glioblastoma (BELOB trial): a randomised controlled phase 2 trial. Lancet Oncol 2014;15:943–53 [PubMed: 25035291]
7. Casanovas O, Hicklin DJ, Bergers G, Hanahan D. Drug resistance by evasion of antiangiogenic targeting of VEGF signaling in late-stage pancreatic islet tumors. Cancer Cell 2005;8:299–309 [PubMed: 16226705]
8. Yamamoto Y, Tamura R, Tanaka T, Ohara K, Tokuda Y, Miyake K, et al. "Paradoxical" findings of tumor vascularity and oxygenation in recurrent glioblastomas refractory to bevacizumab. Oncotarget 2017;8:103890–9 [PubMed: 29262608]
9. Kuang R, Jahangiri A, Mascharak S, Nguyen A, Chandra A, Flanigan PM, et al. GLUT3 upregulation promotes metabolic reprogramming associated with antiangiogenic therapy resistance. JCI Insight 2017;2:e88815 [PubMed: 28138554]
10. Hu YL, DeLay M, Jahangiri A, Molinaro AM, Rose SD, Carbonell WS, et al. Hypoxia-induced autophagy promotes tumor cell survival and adaptation to antiangiogenic treatment in glioblastoma. Cancer research 2012;72:1773–83 [PubMed: 22447568]
11. Jahangiri A, Nguyen A, Chandra A, Sidorov MK, Yagnik G, Rick J, et al. Cross-activating c-Met/beta1 integrin complex drives metastasis and invasive resistance in cancer. Proc Natl Acad Sci U S A 2017;114:E8685–E94 [PubMed: 28973887]
12. Savas P, Teo ZL, Lefevre C, Flensburg C, Caramia F, Alsop K, et al. The Subclonal Architecture of Metastatic Breast Cancer: Results from a Prospective Community-Based Rapid Autopsy Program "CASCADE". PLoS Med 2016;13:e1002204 [PubMed: 28027312]
13. Carbonell WS, De Lay M, Jahangiri A, Park CC, Aghi MK. β1 integrin targeting potentiates antiangiogenic therapy and inhibits the growth of bevacizumab-resistant glioblastomas. Cancer Research 2013;73:3145–54 [PubMed: 23644530]
14. Jahangiri A, De Lay M, Miller LM, Carbonell WS, Hu YL, Lu K, et al. Gene expression profile identifies tyrosine kinase c-Met as a targetable mediator of antiangiogenic therapy resistance. Clinical cancer research : an official journal of the American Association for Cancer Research 2013;19:1773–83 [PubMed: 23307858]
15. Shi L, Chen J, Yang J, Pan T, Zhang S, Wang Z. MiR-21 protected human glioblastoma U87MG cells from chemotherapeutic drug temozolomide induced apoptosis by decreasing Bax/Bcl-2 ratio and caspase-3 activity. Brain Res 2010;1352:255–64 [PubMed: 20633539]
16. Satija R, Farrell JA, Gennert D, Schier AF, Regev A. Spatial reconstruction of single-cell gene expression data. Nature Biotechnology 2015;33:495
17. Muller S, Cho A, Liu SJ, Lim DA, Diaz A. CONICS integrates scRNA-seq with DNA sequencing to map gene expression to tumor sub-clones. Bioinformatics 2018
18. Kwon AT, Arenillas DJ, Worsley Hunt R, Wasserman WW. oPOSSUM-3: advanced analysis of regulatory motif over-representation across genes or ChIP-Seq datasets. G3 (Bethesda) 2012;2:987–1002 [PubMed: 22973536]
19. DeLay M, Jahangiri A, Carbonell WS, Hu YL, Tsao S, Tom MW, et al. Microarray analysis verifies two distinct phenotypes of glioblastomas resistant to antiangiogenic therapy. Clin Cancer Res 2012;18:2930–42 [PubMed: 22472177]

20. McLachlan GJ, Bean RW, Jones LB. A simple implementation of a normal mixture approach to differential gene expression in multiclass microarrays. Bioinformatics 2006;22:1608–15 [PubMed: 16632494]
21. Barry WT, Nobel AB, Wright FA. A statistical framework for testing functional categories in microarray data. Ann Appl Stat 2008;2:286–315
22. Phillips HS, Kharbanda S, Chen R, Forrest WF, Soriano RH, Wu TD, et al. Molecular subclasses of high-grade glioma predict prognosis, delineate a pattern of disease progression, and resemble stages in neurogenesis. Cancer Cell 2006;9:157–73 [PubMed: 16530701]
23. Lin JG, Kang CC, Zhou Y, Huang H, Herr AE, Kumar S. Linking invasive motility to protein expression in single tumor cells. Lab Chip 2018;18:371–84 [PubMed: 29299576]
24. Rahbari NN, Kedrin D, Incio J, Liu H, Ho WW, Nia HT, et al. Anti-VEGF therapy induces ECM remodeling and mechanical barriers to therapy in colorectal cancer liver metastases. Science Translational Medicine 2016;8:360ra135–360ra135
25. Wolf KJ, Lee S, Kumar S. A 3D topographical model of parenchymal infiltration and perivascular invasion in glioblastoma. APL Bioeng 2018;2
26. Calabrese C, Poppleton H, Kocak M, Hogg TL, Fuller C, Hamner B, et al. A perivascular niche for brain tumor stem cells. Cancer Cell 2007;11:69–82 [PubMed: 17222791]
27. Mori H, Ninomiya K, Kino-oka M, Shofuda T, Islam MO, Yamasaki M, et al. Effect of neurosphere size on the growth rate of human neural stem/progenitor cells. J Neurosci Res 2006;84:1682–91 [PubMed: 17044035]
28. Edwards LA, Li A, Berel D, Madany M, Kim NH, Liu M, et al. ZEB1 regulates glioma stemness through LIF repression. Sci Rep 2017;7:69 [PubMed: 28246407]
29. Masin M, Vazquez J, Rossi S, Groeneveld S, Samson N, Schwalie PC, et al. GLUT3 is induced during epithelial-mesenchymal transition and promotes tumor cell proliferation in non-small cell lung cancer. Cancer Metab 2014;2:11 [PubMed: 25097756]
30. Larsen JE, Nathan V, Osborne JK, Farrow RK, Deb D, Sullivan JP, et al. ZEB1 drives epithelial-to-mesenchymal transition in lung cancer. J Clin Invest 2016;126:3219–35 [PubMed: 27500490]
31. Okamoto T, Suzuki K. The Role of Gap Junction-Mediated Endothelial Cell-Cell Interaction in the Crosstalk between Inflammation and Blood Coagulation. Int J Mol Sci 2017;18
32. Avtanski DB, Nagalingam A, Bonner MY, Arbiser JL, Saxena NK, Sharma D. Honokiol inhibits epithelial-mesenchymal transition in breast cancer cells by targeting signal transducer and activator of transcription 3/Zeb1/E-cadherin axis. Mol Oncol 2014;8:565–80 [PubMed: 24508063]
33. Miller K, Wang M, Gralow J, Dickler M, Cobleigh M, Perez EA, et al. Paclitaxel plus bevacizumab versus paclitaxel alone for metastatic breast cancer. N Engl J Med 2007;357:2666–76 [PubMed: 18160686]
34. Jain RK. Normalizing tumor vasculature with anti-angiogenic therapy: a new paradigm for combination therapy. Nat Med 2001;7:987–9 [PubMed: 11533692]
35. Tolaney SM, Boucher Y, Duda DG, Martin JD, Seano G, Ancukiewicz M, et al. Role of vascular density and normalization in response to neoadjuvant bevacizumab and chemotherapy in breast cancer patients. Proc Natl Acad Sci U S A 2015;112:14325–30 [PubMed: 26578779]
36. Heist RS, Duda DG, Sahani DV, Ancukiewicz M, Fidias P, Sequist LV, et al. Improved tumor vascularization after anti-VEGF therapy with carboplatin and nab-paclitaxel associates with survival in lung cancer. Proc Natl Acad Sci U S A 2015;112:1547–52 [PubMed: 25605928]
37. Hirata E, Yukinaga H, Kamioka Y, Arakawa Y, Miyamoto S, Okada T, et al. In vivo fluorescence resonance energy transfer imaging reveals differential activation of Rho-family GTPases in glioblastoma cell invasion. Journal of cell science 2012;125:858–68 [PubMed: 22399802]
38. Baker GJ, Yadav VN, Motsch S, Koschmann C, Calinescu AA, Mineharu Y, et al. Mechanisms of glioma formation: iterative perivascular glioma growth and invasion leads to tumor progression, VEGF-independent vascularization, and resistance to antiangiogenic therapy. Neoplasia 2014;16:543–61 [PubMed: 25117977]
39. Diksin M, Smith SJ, Rahman R. The Molecular and Phenotypic Basis of the Glioma Invasive Perivascular Niche. Int J Mol Sci 2017;18

40. Rubenstein JL, Kim J, Ozawa T, Zhang M, Westphal M, Deen DF, et al. Anti-VEGF antibody treatment of glioblastoma prolongs survival but results in increased vascular cooption. Neoplasia 2000;2:306–14 [PubMed: 11005565]
41. Goel Hira L, Pursell B, Shultz Leonard D, Greiner Dale L, Brekken Rolf A, Vander Kooi Craig W, et al. P-Rex1 Promotes Resistance to VEGF/VEGFR-Targeted Therapy in Prostate Cancer. Cell Reports 2016;14:2193–208 [PubMed: 26923603]
42. Keunen O, Johansson M, Oudin A, Sanzey M, Rahim SA, Fack F, et al. Anti-VEGF treatment reduces blood supply and increases tumor cell invasion in glioblastoma. Proc Natl Acad Sci U S A 2011;108:3749–54 [PubMed: 21321221]
43. Carbone C, Moccia T, Zhu C, Paradiso G, Budillon A, Chiao PJ, et al. Anti-VEGF treatment-resistant pancreatic cancers secrete proinflammatory factors that contribute to malignant progression by inducing an EMT cell phenotype. Clin Cancer Res 2011;17:5822–32 [PubMed: 21737511]
44. Piao Y, Liang J, Holmes L, Henry V, Sulman E, de Groot JF. Acquired resistance to anti-VEGF therapy in glioblastoma is associated with a mesenchymal transition. Clin Cancer Res 2013;19:4392–403 [PubMed: 23804423]
45. Verhaak RG, Hoadley KA, Purdom E, Wang V, Qi Y, Wilkerson MD, et al. Integrated genomic analysis identifies clinically relevant subtypes of glioblastoma characterized by abnormalities in PDGFRA, IDH1, EGFR, and NF1. Cancer Cell 2010;17:98–110 [PubMed: 20129251]
46. Bhat KPL, Balasubramaniyan V, Vaillant B, Ezhilarasan R, Hummelink K, Hollingsworth F, et al. Mesenchymal differentiation mediated by NF-kappaB promotes radiation resistance in glioblastoma. Cancer cell 2013;24:331–46 [PubMed: 23993863]
47. Sequist LV, Waltman BA, Dias-Santagata D, Digumarthy S, Turke AB, Fidias P, et al. Genotypic and histological evolution of lung cancers acquiring resistance to EGFR inhibitors. Sci Transl Med 2011;3:75ra26
48. Boisen MK, Madsen CV, Dehlendorff C, Jakobsen A, Johansen JS, Steffensen KD. The Prognostic Value of Plasma YKL-40 in Patients With Chemotherapy-Resistant Ovarian Cancer Treated With Bevacizumab. Int J Gynecol Cancer 2016;26:1390–8 [PubMed: 27648712]
49. Boisen MK, Holst CB, Consalvo N, Chinot OL, Johansen JS. Plasma YKL-40 as a biomarker for bevacizumab efficacy in patients with newly diagnosed glioblastoma in the phase 3 randomized AVAglio trial. Oncotarget 2018;9:6752–62 [PubMed: 29467925]
50. Wen PY, Prados M, Chamberlain M, Cloughesy TF, Drappatz J, Mikkelsen T, et al. A Phase 2 Study of XL184, an Inhibitor of Met, VEGFR2, and RET, in patients with progressive glioblastoma multforme. 2009; New Orleans, LA.

STATEMENT OF SIGNIFICANCE

Bevacizumab resistance in glioblastoma (GBM) is associated with mesenchymal/glycolytic shifts involving YKL-40 and ZEB1. Targeting ZEB1 reduces bevacizumab-resistant GBM phenotypes.

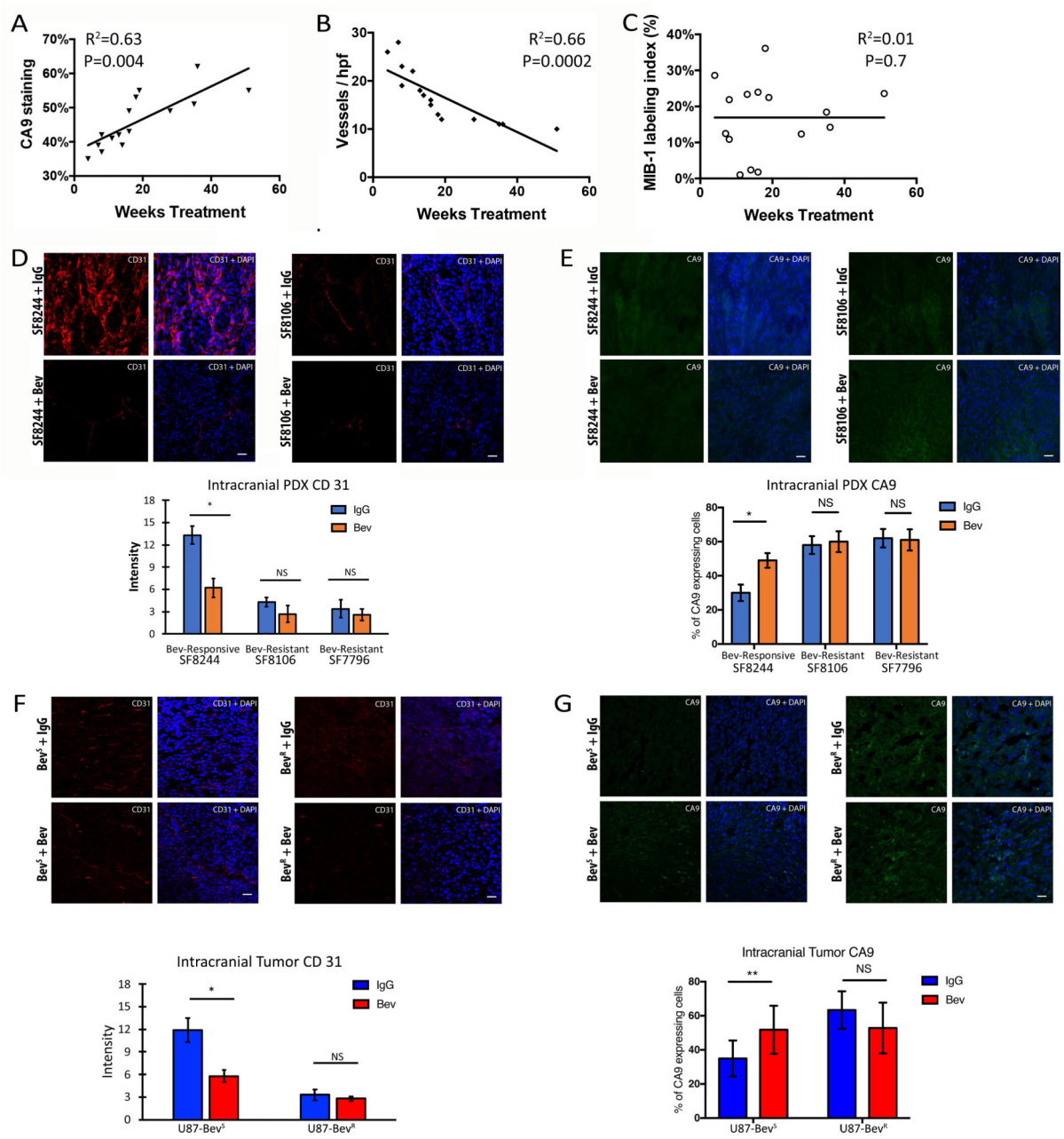

Figure 1. BRGs grow despite successful bevacizumab-induced tumor devascularization and hypoxia in patients and two xenograft models.

(**a**) Increased CA9 staining (R^2=0.63; P=0.004; nonlinear regression), (**b**) decreased vessel density (R^2=0.66; P=0.0002; nonlinear regression), and (**c**) unchanged proliferation (R^2=0.01; P=0.7; nonlinear regression) were seen with increased duration of bevacizumab treatment in patient BRGs (n=15). (**d-e**) Similarly, intracranial bevacizumab-responsive PDXs (SF8244) exhibited decreased vessel density (P=0.02; t-test) and increased hypoxia (P=0.01; t-test) in response to bevacizumab but bevacizumab-resistant PDXs (SF7796 and SF8106) were devascularized and hypoxic at baseline and those parameters did not change in response to bevacizumab (P=0.5–0.9; t-test) (n=3 tumors/group and 5 images/tumor). (**f-**

g) Corroborative xenograft evidence was found in a second model in which decreased vessel density (P=0.03; t-test) and increased hypoxia (P=0.001; t-test) were noted with bevacizumab treatment of intracranial bevacizumab-responsive U87-Bev^{S} xenografts, while intracranial bevacizumab-resistant U87-Bev^{R} xenografts were devascularized and hypoxic at baseline and those parameters did not change in response to bevacizumab (P=0.1–0.6; t-test). n=3 tumors/group and 5 images/tumor, 20x magnification, scale bar=20μm.

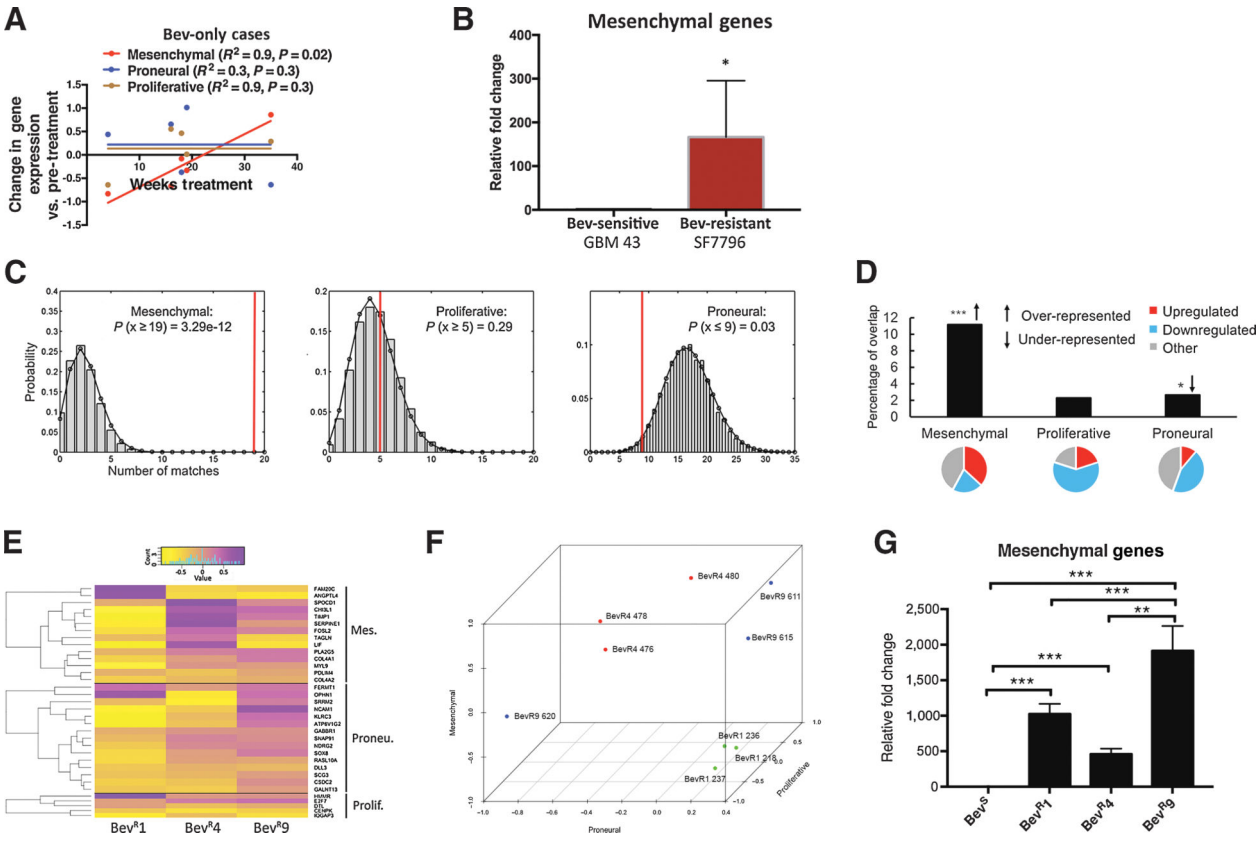

Figure 2. BRGs exhibit increased mesenchymal gene expression in patients and two xenograft models.

(**a**) Increased mesenchymal gene expression (R^2=0.9; P=0.02) and no change in proneural (R^2=0.3; P=0.3) or proliferative (R^2=0.9; P=0.3) gene expression were seen with increased duration of bevacizumab monotherapy treatment in patient BRGs (n=5; nonlinear regression). (**b**) Mesenchymal gene upregulation was confirmed by qPCR in a bevacizumab-resistant (SF7796) relative to a bevacizumab-responsive (GBM43) PDX (n=3/group; P=0.03; t-test). (**c-d**) Bootstrapping analysis of microarray data revealed the Philips mesenchymal gene set to be highly over-represented and proneural gene set to be under-represented among genes significantly dysregulated across U87-Bev^R generations (see Supplementary Methods; n=3/group), with 19/170 (11%) mesenchymal genes and 9/338 (2%) proneural genes dysregulated. 37% of dysregulated mesenchymal genes were upregulated, while 44% of dysregulated proneural genes were downregulated. (**e**) Heatmap analysis of microarray data revealed increased mesenchymal gene expression with increasing U87-Bev^R generation (n=3/group). (**f**) Heatmap expression of signature mesenchymal, proneural, and proliferative genes were normalized and plotted on a −1 to +1 scale, revealing increased mesenchymal gene expression approaching +1 by generation 4 and persisting thereafter (n=3/group). (**g**) Mesenchymal gene upregulation was confirmed by qPCR in U87-Bev^R relative to U87-Bev^S xenografts (P<0.001 and P<0.01; n=6/group; t-test).

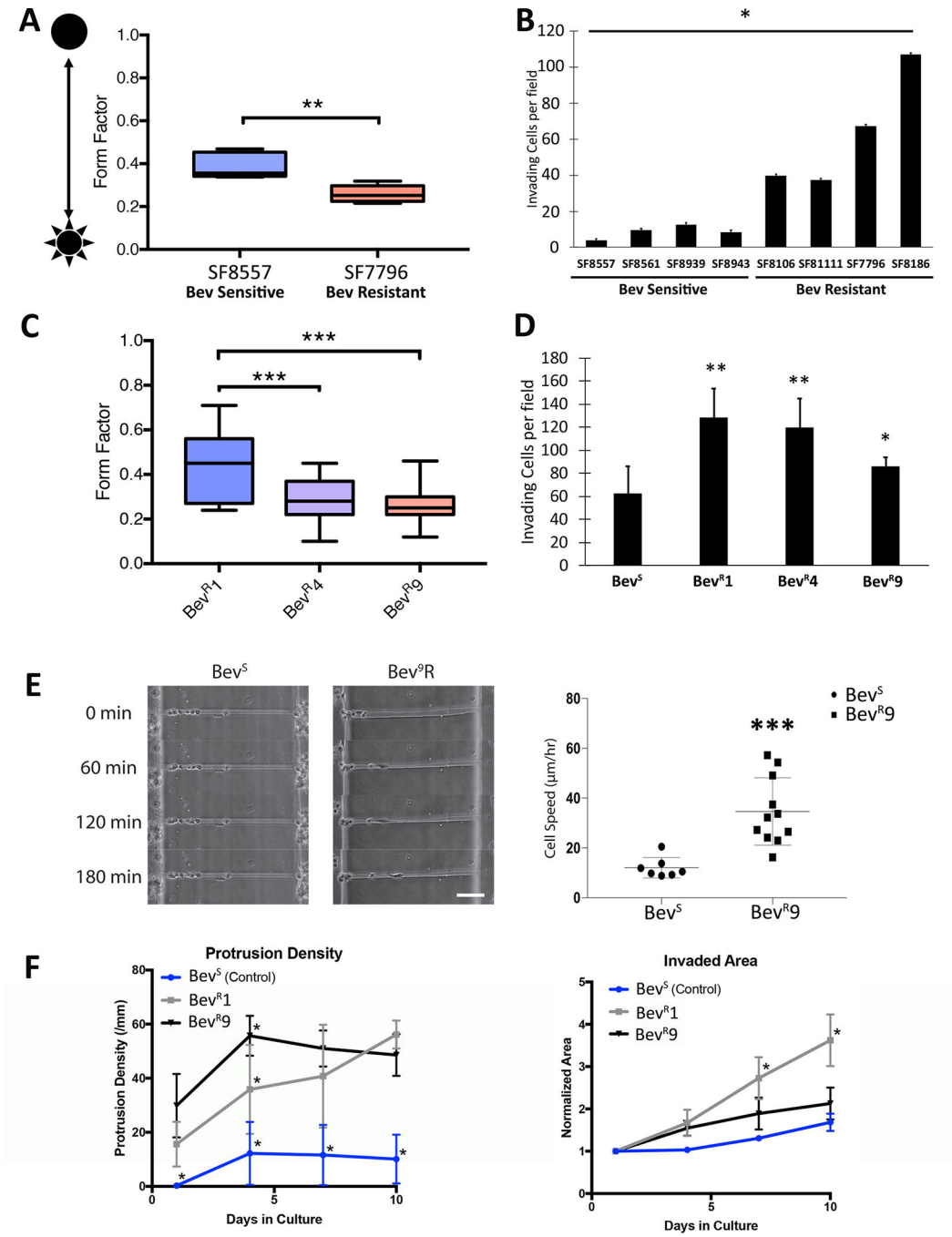

Figure 3. Xenograft models of bevacizumab resistance replicate patient BRG invasiveness

(**a**) Morphological analysis of PDX cells reveals lower form factor in bevacizumab-resistant PDX SF7796 cells compared to bevacizumab-naïve PDX SF8557 cells (n=50/group; P=0.02; t-test). (**b**) Matrigel invasion assay reveals higher invasiveness of bevacizumab-resistant PDX cells compared to bevacizumab-responsive PDX cells (n=6/group; P=0.04; ANOVA). (**c**) Morphological analysis of generations 1,4 and 9 of U87-Bev^R reveals lower form factor associated with generations 4 and 9 of U87-Bev^R (n=50/group; P=0.0009 and P=0.0006, t-test) (**d**) Matrigel invasion assay reveals higher invasiveness of multiple U87-

Bev^R generations versus U87-Bev^S (n=6/group; P=0.02–0.007, t-test) (**e**) 3D bioengineered hydrogel assay modeling white matter tracts and (**f**) 3D bioengineered microchannel platform modeling perivascular invasion revealed higher invasiveness (P<0.001 hydrogel and P<0.05 microchannel; n=3–4 independent devices per condition; ANOVA) of multiple U87-Bev^R generations vs. U87-Bev^S cells. 10x magnification, Scale bar=100 μm. *P<0.05, **P<0.01, ***P<0.001.

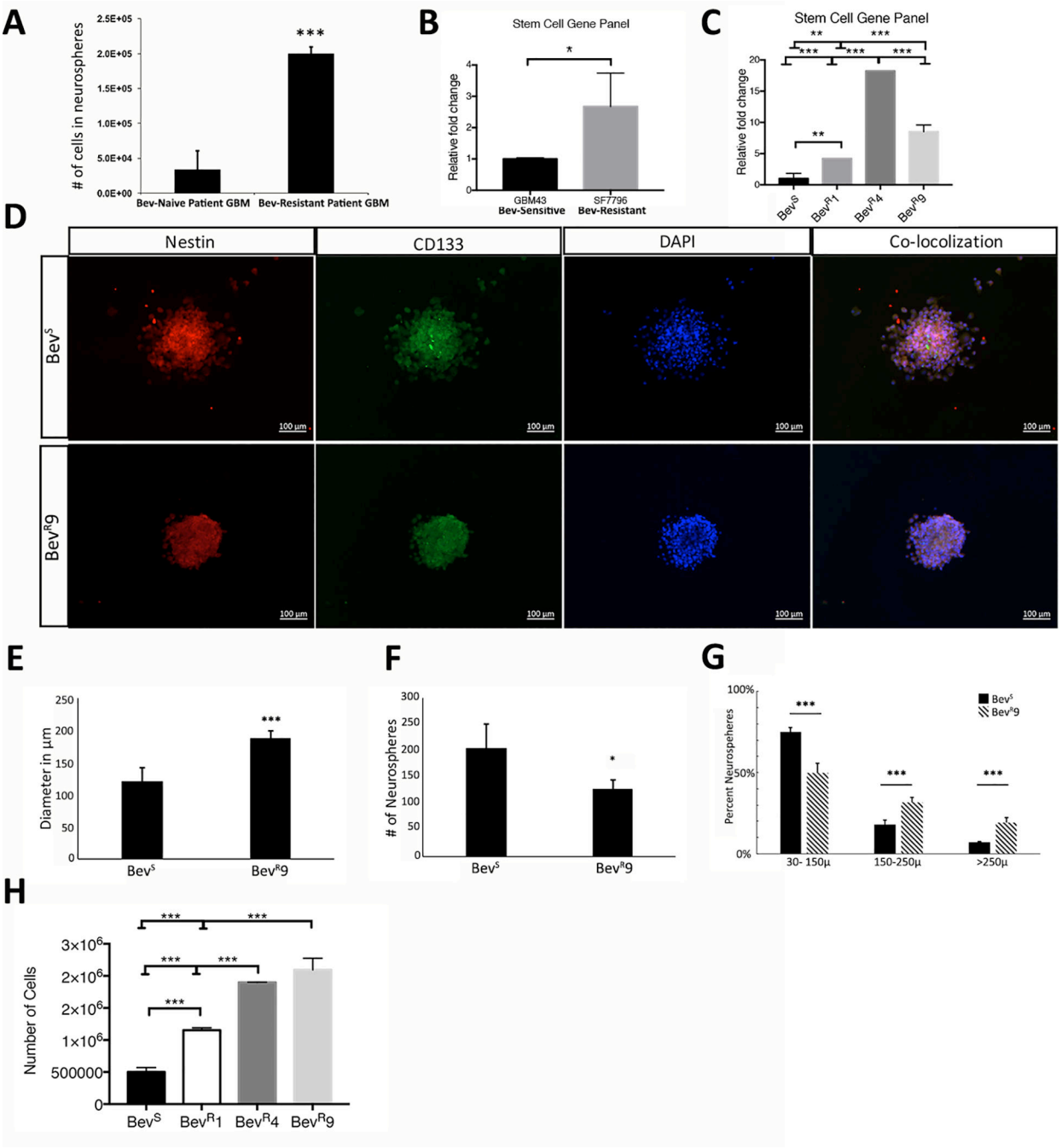

Figure 4. BRG stem cell-enrichment in patients and two xenograft models.

(**a**) Higher total stem cell count yield from neurospheres derived from bevacizumab-resistant patient tumors (n=5) compared to bevacizumab-naïve patient tumors (n=5) (P=0.0004; t-test). (**b**) Increased expression of GBM stemness genes in bevacizumab-resistant GBM by qPCR in PDX models (n=3/group; P=0.02; t-test). (**c**) Increased expression of GBM stemness genes in bevacizumab-resistant GBM by qPCR in our multigenerational resistance model (n=3/group; P=0.0004–0.02; t-test). (**d**) Immunofluorescent staining of neurospheres derived from U87-Bev^{S} and U87-Bev^{R} generation 9 cells was done with Nestin and CD133

(stem cell markers). 20x magnification; scale bar=100μm. (**e**) Neurosphere formation assay revealed larger diameter of U87-Bev^R generation 9 neurospheres (n=6/group; P=0.0002; t-test), while Bev^S cells yielded a larger number of neurospheres (n=6/group; P=0.03; t-test). (**f**) Neurosphere formation assay revealed a lower number of neurospheres from Bev^R generation 9 cells compared to Bev^S cells (n=6/group; P=0.03; t-test). (**g**) Relative distribution of Bev^S and Bev^R generation 9 neurospheres by diameter size reveals larger Bev^R generation 9 neurospheres (n=6/group; P<0.001; t-test). (**h**) Absolute cell counts from U87-Bev^S and U87-Bev^R generations 1,4,9 neurospheres (n=6/group P<0.001 for all comparisons; t-test). *P<0.05, **P<0.01, ***P<0.001.

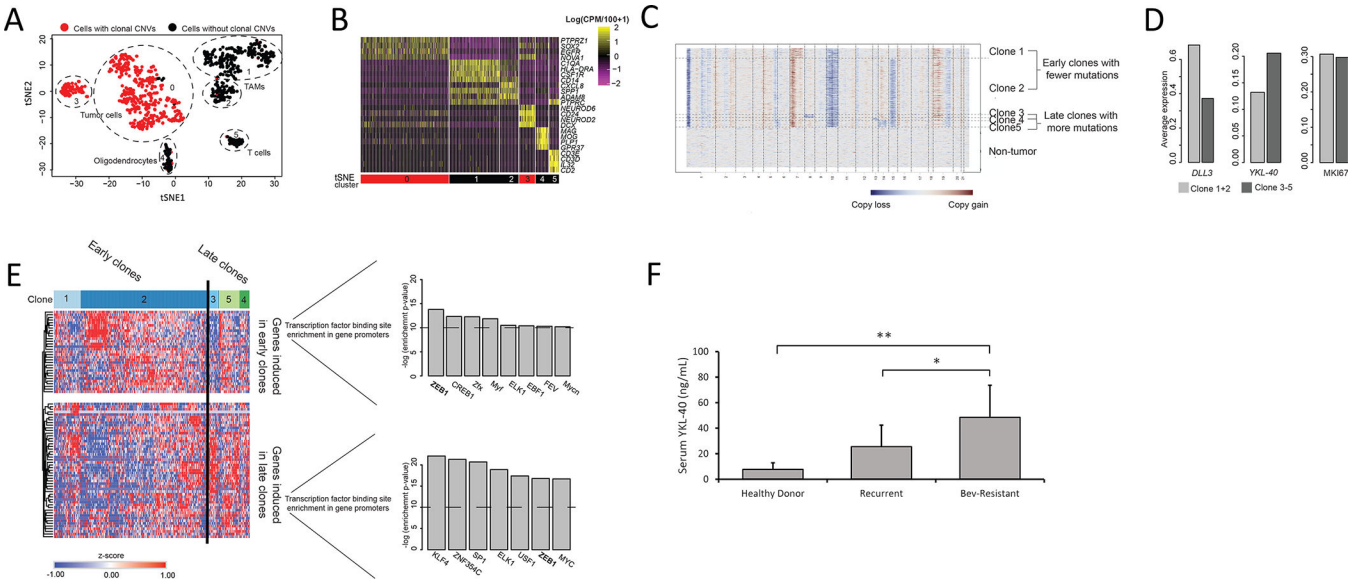

Figure 5. Single-cell patient BRG sequencing reveals clonal evolution of mesenchymal resistance and identifies a circulating resistance biomarker.

(**a**) Single-cell RNA sequencing of 857 cells from a BRG reveals clusters of single cells representing BRG cells that differ in the expression of these genes as represented in the t-SNE plot. To generate the dimensionality-reduced representation, only the 500 genes most strongly differentially expressed between bevacizumab-resistant and pre-resistance samples of GBM cases from our previous study were used. (**b**) Heatmap of the 24 most significantly enriched genes (rows) in all cells in each cluster (columns) reveals BRG cells (cluster 0 and 3) have a higher expression of mesenchymal genes compared to non-malignant cell types. (**c**) Heatmap visualizing average gene expression along chromosomes (x-axis) for all cells (y-axis). Non-tumor cells (bottom) lack copy number alterations, while malignant cells harbor multiple large-scale CNVs, including glioma typical gain of Chr7 and loss of Chr10, and reveal 5 clones of BRGs. (**d**) Comparing expression of mesenchymal vs. proneural genes revealed that mesenchymal genes such as YKL-40 were more upregulated in “late” clones, defined as clones with more mutations, than “early” clones, defined as those with fewer mutations. (**e**) While ZEB1 binding is enriched in genes upregulated in early and late clones, because the enrichment p-value is more significant in late clones, ZEB1 drives expression of genes especially in late, presumably more resistant clones. (**f**) ELISA reveals elevated YKL-40 levels in patients with GBMs resistant to bevacizumab (n=8) vs. patients with recurrent bevacizumab-naïve GBM (n=11) (P=0.02, t-test) and healthy donors (n=3) (P=0.007, t-test). *P<0.05, **P<0.01, ***P<0.001

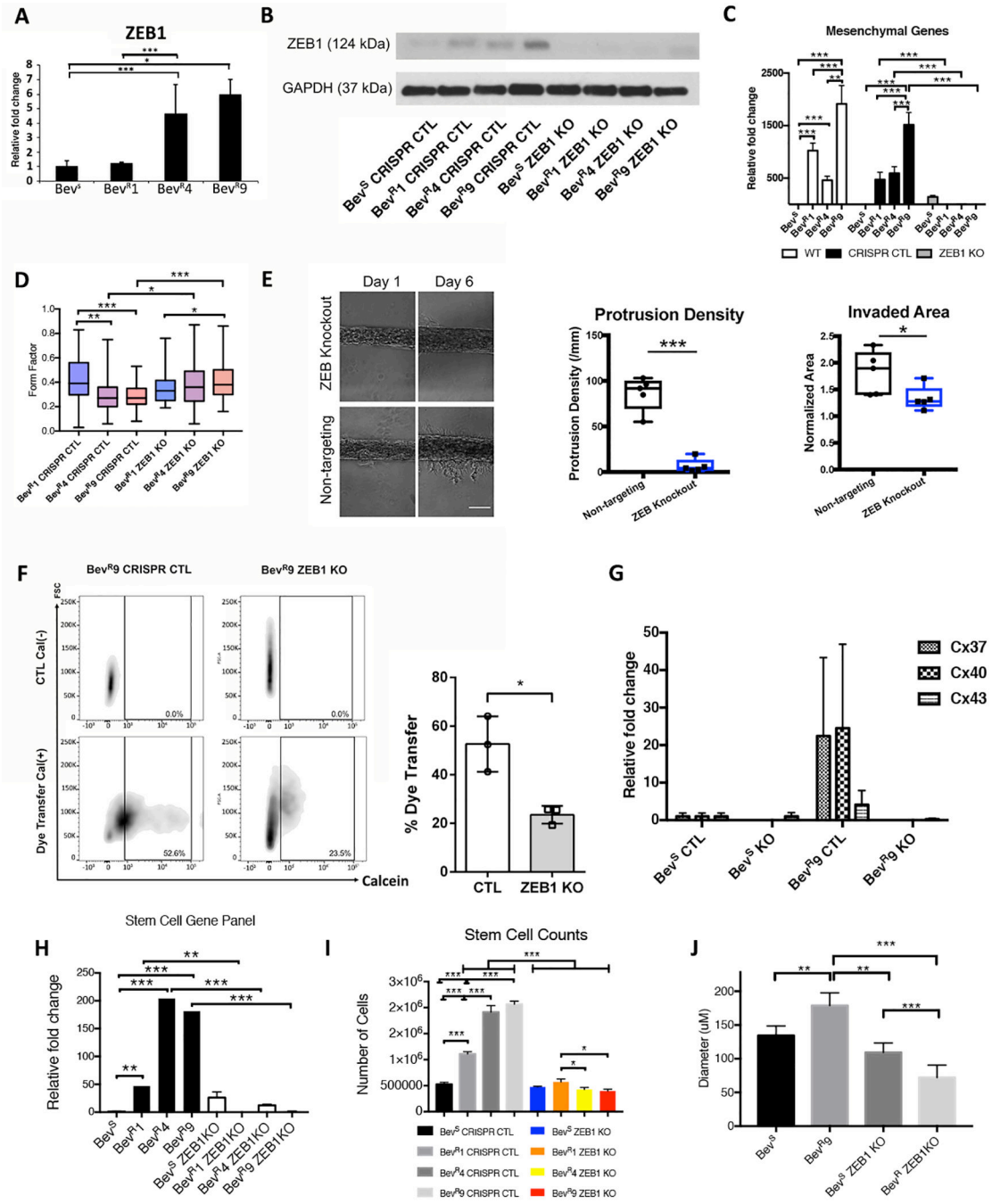

Figure 6. ZEB1 drives the mesenchymal phenotype in bevacizumab-resistant GBM.

(**a**) Transcriptional ZEB1 analysis in tumor chunks from U87-Bev^S generation 9, U87-Bev^R generation 1, 4 and 9 reveals a positive correlation between generation number and ZEB1 mRNA expression in U87-Bev^R. For ZEB1, U87-Bev^S vs U87-Bev^R generation 4 and U87-Bev^S vs U87-Bev^R generation 9, $p<0.001$ and 0.02, respectively (n=6/group; t-test). (**b**) ZEB1 knockout (KO) in U87-Bev^S and U87-Bev^R generations 1,4 and 9 using CRISPR was successful, as evidenced by reduced ZEB1 protein expression assessed by Western blot as compared to unaltered cells and cells expressing CRISPR controls. (**c**) ZEB1 KO in U87-

Bev^S and U87-Bev^R generations 1,4 and 9 reveals reduced transcriptional expression of mesenchymal genes compared to unaltered cells and cells expressing CRISPR controls ($P<0.001$ and $P<0.01$; n=6/group; t-test). (**d**) Quantitative morphology analysis of ZEB1 KO reveals significantly higher form factors in U87-Bev^R generations 4 and 9 compared to cells expressing CRISPR controls, suggesting a loss in mesenchymal morphology with ZEB1 KO (n=50/group; P=0.02–0.0006; t-test). (**e**) 3D bioengineered microchannel platforms modeling perivascular invasion through HA reveal lower cell protrusion ($P<0.001$) and lower invasive area ($P<0.05$) in ZEB1 KO U87-Bev^R cells compared to non-targeting CRISPR controls (n=3–4 biological replicates; ANOVA). 10x magnification, scale bar=100μm. (**f**) Flow cytometric analysis revealed that ZEB1 KO reduces calcein dye transfer between HUVEC donor cells and U87-Bev^R recipient cells (n=3 biological replicates; P=0.01, t-test). (**g**) Transcriptional analysis of U87-Bev^S and U87-Bev^R ZEB1 KO cells revealed lower expression of connexins 37, 40 and 43 in ZEB1 KO cells vs. controls ($P<0.001$ for all connexins). ZEB1 KO in U87-Bev^R also decreased (**h**) gene expression of a stem cell panel (n=6/group; P=0.0002–0.003, t-test); (**i**) stem cell counts (n=6/group; P=0.0003–0.02; t-test); and (**j**) stem cell diameters (n=6/group; P=0.0005–0.003; t-test). *$P<0.05$, **$P<0.01$, ***$P<0.001$.

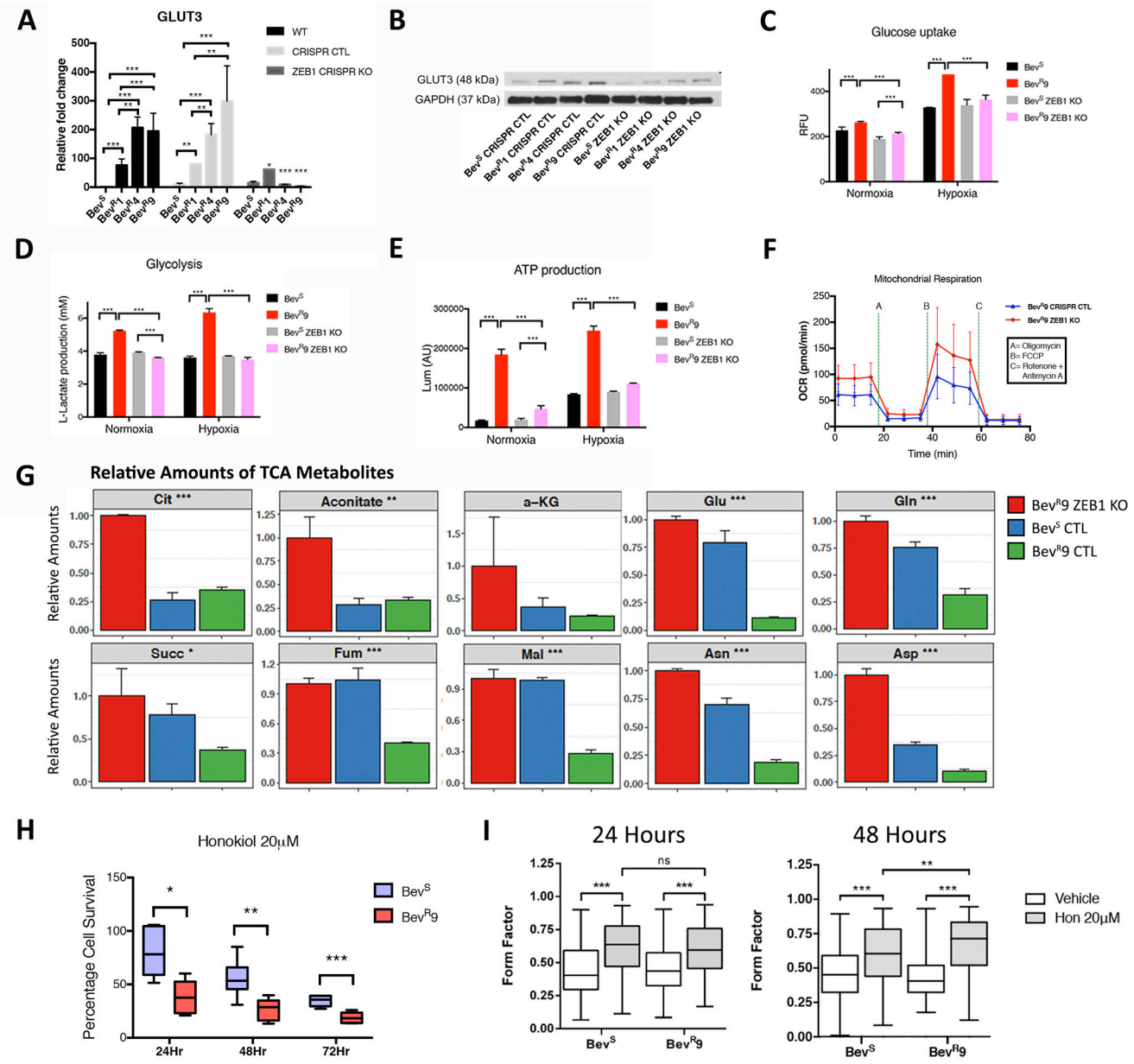

Figure 7. ZEB1 drives metabolic changes associated with bevacizumab resistance.

(**a-b**) ZEB1 CRISPR reduced GLUT3 expression of U87-Bev^R cells assessed by (**a**) qPCR (n=6/group; P<0.05 for generation 1; P<0.001 for generations 4 and 9; t-test) and (**b**) western blot. ZEB1 knockout in U87-Bev^R also caused (**c**) decreased glucose uptake (n=6/group; P<0.001; t-test), (**d**) decreased glycolysis (n=6/group; P<0.001; t-test), and (**e**) decreased ATP production (n=6/group; P<0.001; t-test). (**f**) To assess mitochondrial oxidative phosphorylation, oxygen consumption rate (OCR) were measured over time after treatment with three mitochondrial inhibitors, per the Seahorse extracellular flux analyzer protocol: Oligomycin (injection A; 18 minutes), FCCP (injection B; 36 minutes), and Rotenone+Antimycin A (injection C; 54 minutes). ZEB1 knockout vis CRISPR raised basal respiration (rate before injection 1 minus nonmitochondrial respiration; P=0.002; t-test) and

maximal respiration (non-mitochondrial respiration minus FCCP rate; P=0.008; t-test) in U87-Bev^R cells (n=12/condition and time point). (**g**) Incubating cells in a low concentration (0.1 g/L) of $^{13}C_6$-glucose revealed elevated levels of the 7 most downstream of 10 TCA metabolites in U87-Bev^S cells that were lost in U87-Bev^R cells but regained when U87-Bev^R cells expressed ZEB1 CRISPR (asterisks=ANOVA results with subsequent pairwise analysis: P>0.05 U8/-Bev^R/ZEB KO vs. U87-Bev^S/CTL and P<0.05 between each of these and U87-Bev^R/CTL. (**h**) Trypan blue viability assay revealed that 20 μM Honokiol increased cell death in U87-Bev^R (generation 9) cells versus U87-Bev^S cells with 50% fewer viable bevacizumab-resistant than bevacizumab-sensitive cells at 24 (38% vs 77%; p<0.05), 48 (27% vs 55%; P<0.01) and 72 hours (19% vs 35%; P<0.001) (n=6/group; t-test). (**i**) Quantitative morphology analysis revealed that honokiol raised form factors of U87-Bev^S and U87-Bev^R (generation 9) cells (n=50/group; P<0.001, t-test), suggesting lost mesenchymal morphology in cells surviving honokiol-mediated ZEB1 inhibition. *P<0.05, **P<0.01, ***P<0.001.